Received: 29 May 2020 | Revised: 19 July 2020 | Accepted: 19 July 2020

DOI: 10.1002/er.5863

RESEARCH ARTICLE

INTERNATIONAL JOURNAL OF ENERGY RESEARCH WILEY

Geometrical effects on ionic diffusion in carbon-carbon symmetric supercapacitors

Wei Sun[1,2] | **Fuqian Yang**[2]

[1]College of Chemistry, Chemical Engineering and Environmental Engineering, Liaoning Shihua University, Fushun, China

[2]Materials Program, Department of Chemical and Materials Engineering, University of Kentucky, Lexington, Kentucky

Correspondence
Fuqian Yang, Materials Program, Department of Chemical and Materials Engineering, University of Kentucky, Lexington, KY 40506.
Email: fyang2@uky.edu

Funding information
National Natural Science Foundation of China, Grant/Award Number: 21805123; National Science Foundation, Grant/Award Number: CMMI-1634540; Talent Scientific Research Fund of LSHU, Grant/Award Number: 2016XJJ-077; LiaoNing Revitalization Talents Program, Grant/Award Number: XLYC1907067

Summary

There is a great need to understand the structural dependence of supercapacitors for the development of advanced electrode materials that can be used to improve the electrochemical performance and structural integrity. In this work, we investigate the effects of the size and pore width/size of activated carbon microspheres (ACMSs) with diameter in a range of 2.7 ± 0.54 to 9.45 ± 1.81 μm and average pore width in a range of 1.60 to 2.0 nm on the electrochemical impedance characteristics of carbon-carbon symmetrical supercapacitors. Both the size and pore width/size of the ACMSs have negligible effects on contact resistance. The activation energy for the migration/diffusion of electrolyte ions in the supercapacitors made from the ACMSs of nearly same porous structure increases nonlinearly with the increase of the average size of the ACMSs, which is likely associated with overscreening effect. The activation energy for the migration/diffusion of electrolyte ions in the supercapacitors made from the ACMSs of nearly same size increases first and then decreases as the pore width/size increases.

KEYWORDS

activated carbon microspheres, activation energy, diffusion coefficient, impedance spectroscopy

1 | INTRODUCTION

Supercapacitor with excellent, comprehensive performance in energy storage has been attracting great interest both in industry and in academia.[1-4] The high rate performance, which is superior to metal-ion batteries, allows supercapacitor to be a potential candidate of advanced energy storage systems. The applications of supercapacitor are dependent on the development of advanced electrode materials and the rational design of electrode, which necessitate fundamental understanding of the processes controlling ionic migration/diffusion and the effects of material structure and composition.

Supercapacitors can be divided generally into two groups; the one, referring to as electric double layer capacitor (EDLC), is based on the migration and accumulation of ions near the surface of electrode materials,[5,6] and the other one, referring to as pseudo-capacitor, is based on the migration and "reversible" Faradic reaction.[7-9] Pseudo-capacitors can exhibit relatively higher Faradic capacitances than EDLCs,[10] and EDLCs exhibit superior long-term cycling stability and rate performance for ultra-fast capacitors.[11,12]

Activated carbons (ACs) have been extensively used in supercapacitor,[13-20] and porous structure is one of the important structural features determining electrochemical characteristics of activated carbonaceous materials. Nano-porous carbonaceous materials possess high surface area with a large amount of adsorption sites for electrolyte ions and have the potential to achieve high specific capacitance.[21-23] Note that the geometrical dimensions and morphology of pores also

play important roles in charge storage.[1,24] Pores inaccessible to electrolyte ions cannot contribute the energy storage through electric double layer; micropores with sizes slightly larger than electrolyte ions can provide plenty of adsorption sites and are the major structure contributing to high specific capacitance; and mesopores with relatively large sizes benefit ion diffusion for fast charging/discharging.[25,26] There exists synergic effect between micropores and mesopores in activated carbonaceous materials on electrochemical performance of supercapacitor.[27]

Zhou and Yang[24] pointed out that "sheet-like structures, such as multilayer graphene, are preferable for EDLCs" in the analysis of dimensional effect on integral capacitance of rectangular structures, which can be attributed to the large amount of active sites available for electrolyte ions and the pathways presented for rapid migration/diffusion of electrolyte ions.[14,28,29] However, AC of spherical shape (ACSs) with considerable surface area can provide mechanical strength likely to maintain structural integrity during electrochemical cycling,[30,31] and the supercapacitors with ACSs as electrode material can exhibit favorable long-term cycling stability and low contact resistance. Also, carbon spheres can be readily produced through hydrothermal synthesis (HTS) at low cost in contrast to the production of graphene, and the size of carbon spheres can be simply controlled as well.[32,33] Thus, ACSs are still preferable for the applications in supercapacitors.

Gas adsorption-desorption is an important technique to characterize the surface area and pore-size distribution of porous materials. Gases of different molecular/atomic sizes have been used in adsorption-desorption isotherm to determine the surface characteristics of porous materials for a range of pores. For example, CO_2 adsorption analysis can provide accurate information for ultramicropores (pores smaller than 0.7 nm)[34] and micropores, while it is not sensitive for the pores larger than 1.5 nm. H_2 is a good candidate for the characterization of the carbonaceous materials prepared for the applications for H_2 adsorption and separation.[35] N_2 adsorption-desorption isotherm provides good accuracy for the surface characteristics of porous materials with pore sizes in both micro- and meso-ranges[35] and is widely used for ACs.[36-38] The N_2 adsorption-desorption isotherm is more suitable to the analysis of porous materials with pore widths larger than 1 or 1.5 nm, through which relatively large electrolyte ions, such as BF_4^-; (0.98 nm) and Et_4N^+ (1.48 nm),[39] migrate.

It is known that the size and porous structure of ACSs play important roles in energy storage.[40] More understanding on the dependence of the electrochemical characteristics of ACSs, such as ionic diffusion, on the size and surface area is still needed to better control the processes for the fabrication of ACSs. The purpose of this work is to investigate the effects of the size and structure of activated carbon microspheres (ACMSs) on the migration/diffusion of electrolyte ions in carbon-carbon symmetric supercapacitor cells in the framework of electrochemical impedance spectroscopy (EIS). ACMSs of different sizes and porous structures were prepared by the combination of an HTS process, a physical activation, and a chemical activation with KOH as chemical agent. Symmetric supercapacitor cells were assembled with electrodes made from the prepared ACMSs. The EIS analyses of the carbon-carbon symmetric supercapacitor cells were performed to determine the effects of the size and pore width of the ACMSs and temperature on the ionic diffusion in the supercapacitor cells. Apparent activation energy for the ionic diffusion was calculated from the experimental results, which has not been discussed in literature. The results presented in this work can shed insight into ionic migration in supercapacitors and structural effects of activated carbonaceous materials on energy storage.

2 | EXPERIMENTAL DETAILS

Following the method given by Sun et al,[41] we prepared aqueous solutions of xylose. The weight ratio of xylose in the aqueous solutions was in a range of 2.5 to 40 wt%. The hydrothermal carbonization of the aqueous solutions was performed at 200°C for 24 hours. For detailed information, see the work by Sun et al[41] The solid product after the hydrothermal carbonization was collected, washed five times with deionized (DI) water, and dried in a vacuum oven at 110°C for 12 hours. The hydro-char was named as HTS-x (x = 40, 20, 10, 5, 2.5) with x representing the weight fraction of xylose in the corresponding aqueous solution.

The dried hydro-char was physically activated at 600°C for 1 hour in a tube furnace with the flow of nitrogen gas. The solid product after the physical activation was named as HC-x (x = 40, 20, 10, 5, 2.5).

Chemical activation of HC-2.5 was then performed with KOH as chemical agent. Prior to chemical activation, the mixtures of HC-2.5 and KOH powder of different mass ratios (KOH to HC-2.5) in a range of 2 to 12 were well mixed and grounded. After the grinding, the mixtures were chemically activated at 800°C for 1 hour in a tube furnace under the protection of N_2 flow. The solid product after the chemical activation was collected, neutralized with dilute hydrochloric acid, washed five times with DI water, and dried at 110°C overnight. The chemically activated solid product was named as AC-*a*

(a = 1, 2, 4, 8, 12) with a representing the mass ratio of KOH to HC-2.5.

We used scanning electron microscopy (SEM) (Hitachi S-4800) and high-resolution transmission electron microscopy (HRTEM) (JEM-2100F) to characterize the morphologies of the HC-xs and AC-*a*s and N_2 adsorption-desorption isotherm to analyze the surface characteristics of the HC-xs and AC-*a*s. The N_2 adsorption-desorption isotherm was carried out on a gas analyzer (Micromeritics surface characterization). Using the Brunauer-Emmett-Teller (BET) method and the density functional theory (DFT), we calculated the surface area. The relative pressure was 0.98 for the calculation of the distribution of pore widths from the DFT theory.

The mixture of the ACMSs (HC-xs and AC-*a*s) and Teflon powder with 9:1 in the mass ratio of ACMSs to Teflon powder was used to prepare the electrode of symmetrical, coin-like cells. The mixture was first heated at 110°C for 30 minutes, and then ground to a thin chip. A rolling machine was used to flatten and thin the chips to ~0.1 mm in thickness. Circular electrode disks of 4 mm in diameter were punched out from the flattened chips. The loading mass per electrode disk was ~6 mg. The cell was assembled with TF4840 (NKK, Japan) as separator and 1 mol/L Et4NBF4 solution in AN as electrolyte.

The EIS analyses of the prepared symmetrical, coin-like supercapacitor cells were performed on an electrochemical workstation (Vertex one, Ivium, Netherlands) in a temperature range of 0 to 60°C. A water bath was used to control the test temperature. The frequency for the EIS analyses was in a range of $10^6 \sim 10^{-2}$ Hz under an open circuit voltage.

3 | RESULTS

Figure 1A-E shows SEM images and size distributions of the HC-xs. All the HC-xs are present in spherical shape, suggesting that the weight fraction of xylose in the aqueous solutions has no effect on the morphology of the hydro-char produced by the combination of the HTS process and the physical activation at 600°C. According to the results given by Kang et al,[42] we can conclude that all the HC-xs are ACMSs. From the SEM images, we analyze the size distributions of the ACMSs for all the HC-xs, as shown in Figure 1. It is evident that the HTS processing of the aqueous solutions produced polydisperse spheres. The average sizes of the ACMSs are 9.45 ± 1.81, 5.79 ± 1.33, 4.91 ± 1.17, 3.69 ± 1.05, and 2.7 ± 0.54 μm for the HC-40, HC-20, HC-10, HC-5, and HC-2.5, respectively. Increasing the weight fraction of xylose in the aqueous solutions increases average size of the ACMSs under the same processing conditions. Note that there is no significant change of the morphologies of the carbon microspheres after the chemical activation, that is, the AC-*a*s exhibit similar morphologies to the HC-2.5.

Figure 2 depicts HRTEM images of the ACMSs of AC-*a*s. For comparison, the HRTEM image of HC-2.5, which was physically activated, is also included in Figure 2. All the AC-*a*s and the HC-2.5 consist of sub-nano-/nano-scale pores, and the AC-*a*s possess much more fraction of sub-nano−/nano-scale pores than the HC-2.5.

The N_2 adsorption-desorption isotherms of the ACMSs are presented in Figure 3A and c. For the ACMSs of HC-xs (Figure 3A), the N_2 adsorption-desorption isotherms nearly overlap each other and exhibit Type I mode, according the IUPAC classification. The initial steep stage is ascribed to the monolayer adsorption on the surface of micropores. In contrast to the ACMSs of HC-xs, the nitrogen adsorption-desorption isotherms of the ACMSs of AC-*a*s do not overlap with each other, while they do exhibit Type I mode. This characteristic suggests the presence of micropores in accord with the HRTEM images, shown in Figure 2. The broad round knees presented in the nitrogen isotherms of the ACMSs of AC-4, AC-8, and AC-12 (Figure 3C) imply wide distributions of pore widths/sizes.

Figure 3B,D presents the distributions of the pore widths of the ACMSs. All the ACMSs of HC-xs possess nearly the same distribution of pore widths/sizes with all pores being micropores, independent of the sizes of the ACMSs. For the ACMSs of AC-*a*s, the characteristic peaks for the distributions of pore widths/sizes are presented at nearly the same widths, suggesting that the peak pore-widths/sizes are relatively independent of the mass ratio of KOH to HC-2.5. However, the difference in the differential pore volume of the corresponding peak pore-widths reveals that the mass ratio of KOH to HC-2.5 used in the chemical activation played an important role in controlling the fraction of the corresponding pores. Increasing the mass ratio of KOH to HC-2.5 increases the fraction of large pores and average pore width/size.

Table 1 summarizes the surface characteristics of the ACMSs prepared in this work. In general, all the ACMSs of HC-xs statistically possess the same S_{BET} and V_{tot}, independent of the sizes of the ACMSs with all pores being micropores. For the ACMSs of AC-*a*s, increasing the mass ratio of KOH to HC-2.5 increases S_{BET}, V_{tot}, and the fraction of mesopores. The ACMSs of AC-12 possessed the largest S_{BET} of 2449 m^2/g and the largest mesopore fraction of 18.7 vol%.

We performed EIS analyses of the carbon-carbon, symmetric supercapacitor cells in order to examine the characteristics of ionic migration/diffusion. In general, the Nyquist plot can consist of three characteristic regions: a semi-circle in the high-frequency region, a

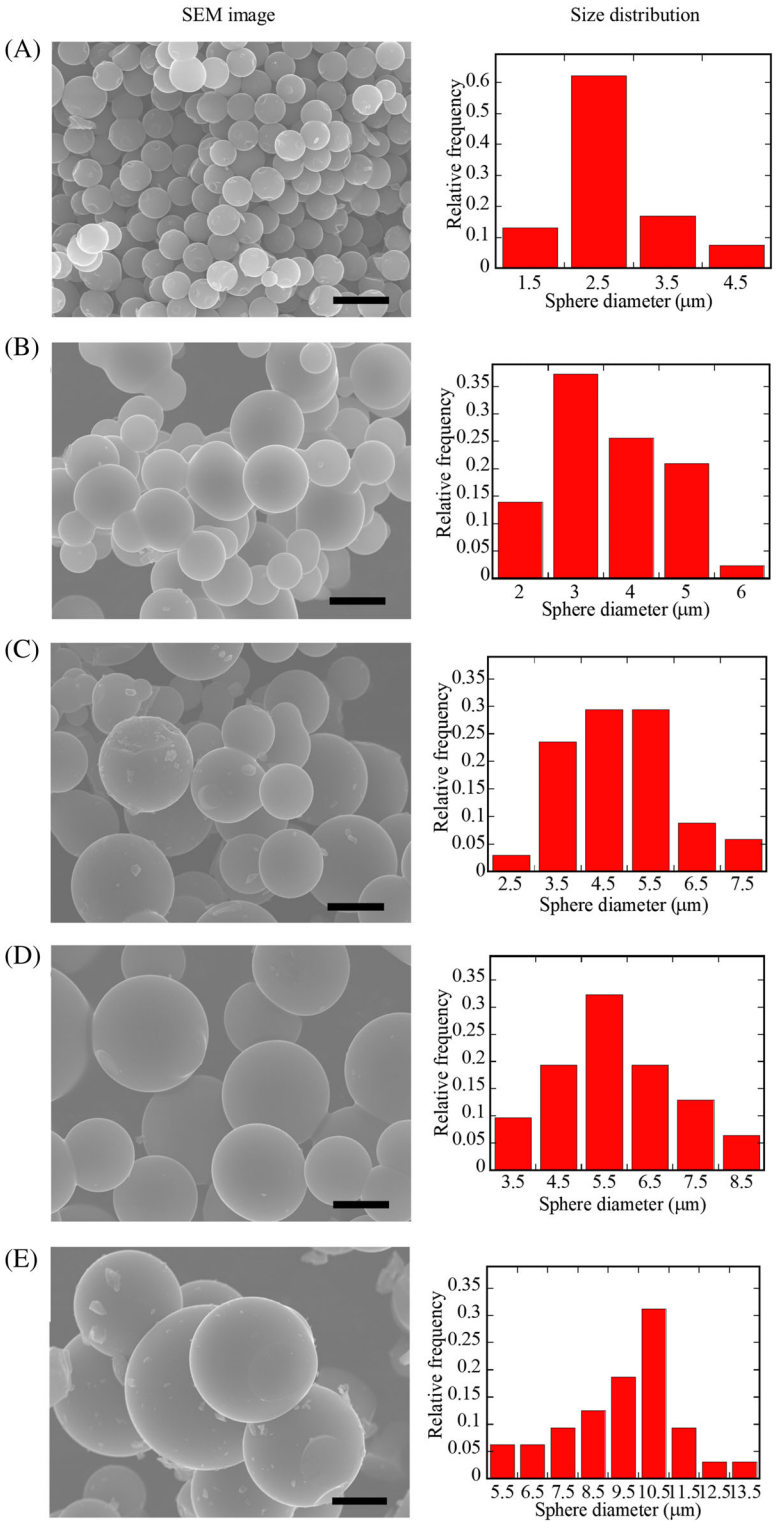

FIGURE 1 SEM image and size distribution of HC-xs. A, HC-2.5. B, HC-5. C, HC-10. D, HC-20. E, HC-40. All the scale bars represent 5 μm [Colour figure can be viewed at wileyonlinelibrary.com]

straight line with ~1 in slope in the intermediate-frequency region, and a steep-straight line close to -z″ axis (z″ is the imaginary part of electrochemical impedance) in the low-frequency range. However, no typical semi-circle is present in the Nyquist plots for all the supercapacitor cells made from the ACMSs, as shown in Figures 4 and 5. Such behavior suggests that it is very difficult to accurately calculate the resistance for charge transfer. Herein, the analysis of the resistance is focused on, R_s, which includes the intrinsic resistances of electrolyte and electrode and the contact resistance between electrode and current collector.

Table 2 lists the resistance, R_s, for the supercapacitor cells made from the ACMSs at different temperatures.

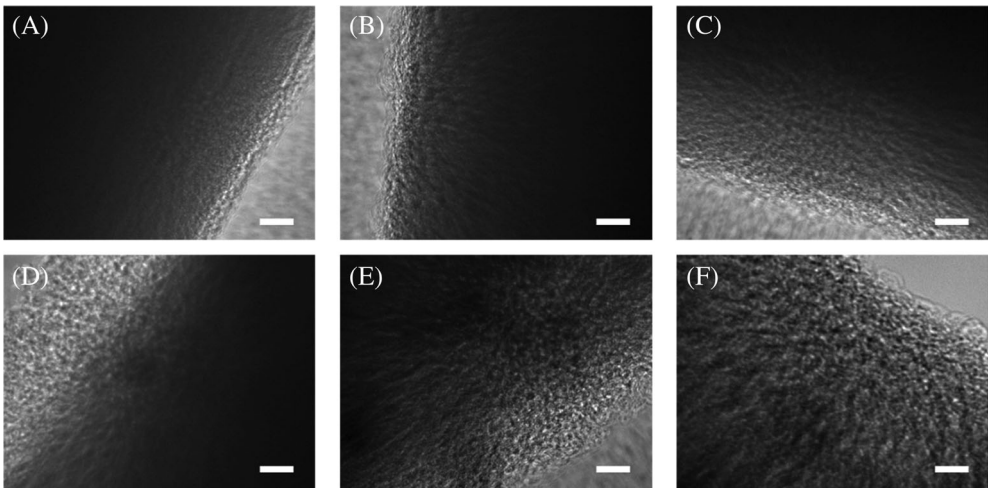

FIGURE 2 HRTEM images of the ACMSs. A, HC-2.5. B, AC-1. C, AC-2. D, AC-4. E, AC-8. F, AC-12. All the scale bars represent 5 nm

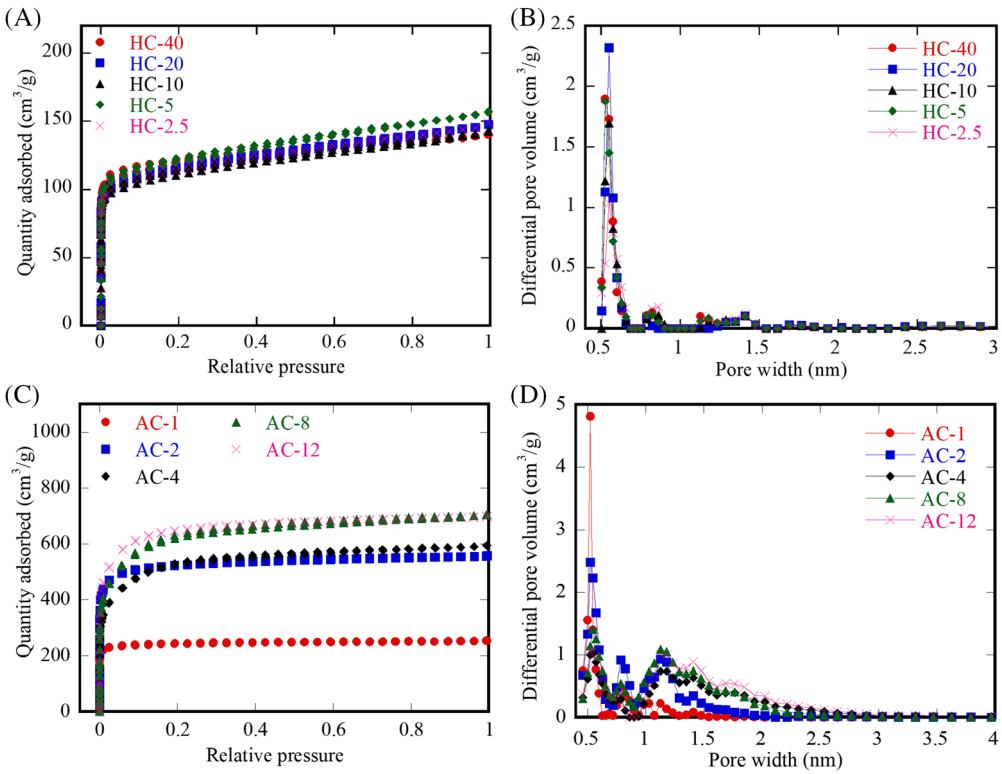

FIGURE 3 N_2 adsorption-desorption isotherms of the ACMSs: A, HC-xs and, C, AC-*as*; pore width distribution of the ACMSs: B, HC-xs and, D, AC-*as* [Colour figure can be viewed at wileyonlinelibrary.com]

TABLE 1 Surface characteristics of the ACMSs

Carbon spheres	S_{BET} (m^2/g)	V_{tot} (cm^3/g)	Micropore (vol%)	Mesopore (vol%)
HC-40	417	0.22	100	0
HC-20	431	0.23	100	0
HC-10	425	0.23	100	0
HC-5	431	0.23	100	0
HC-2.5	452	0.24	100	0
AC-1	974	0.39	99.3	0.7
AC-2	1962	0.86	95.5	4.5
AC-4	2056	0.92	91.2	8.8
AC-8	2327	1.12	83.7	16.3
AC-12	2449	1.24	81.3	18.7

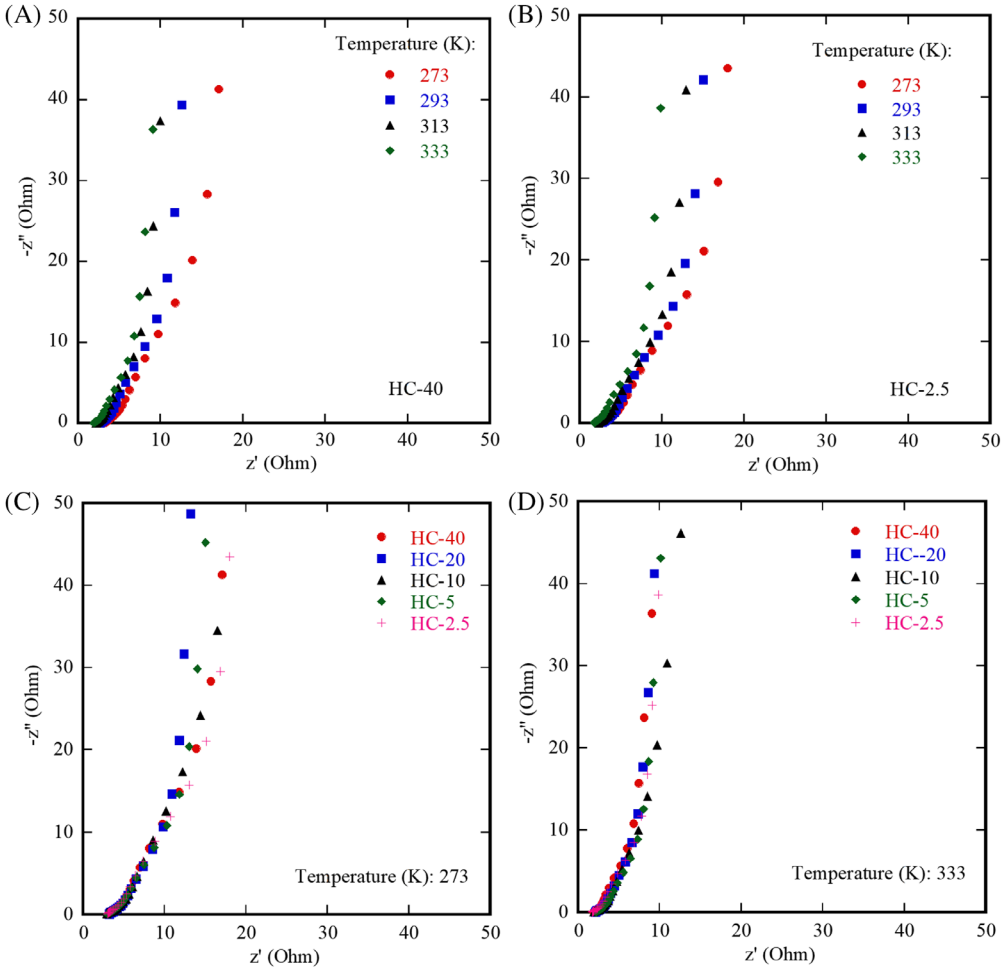

FIGURE 4 Nyquist plots of the symmetrical cells made from the ACMSs of: A, HC-40 and, B, HC-2.5 at different temperatures; Nyquist plots of the symmetrical cells made from the ACMSs of HC-xs at temperatures of: C, 273 K and, D, 333 K [Colour figure can be viewed at wileyonlinelibrary.com]

For the supercapacitor cells made from the ACMSs of HC-xs and AC-*a*s, the R_s value decreases with the increase of temperature, which can be ascribed to the decrease of the electrolyte resistance.[43] Increasing temperature causes the decrease of the electrolyte viscosity and the increase of the migration rate of electrolyte ions under the same driving force. The scattering of the R_s value with the size of the ACMSs of HC-xs and AC-*a*s suggests that the size and pore width/size of the ACMSs has negligible effect on the contact resistance.

From Figure 4, we note that the low-frequency straight lines become steeper with the increase of temperature for the supercapacitors made from the ACMSs of HC-40 (Figure 4A) and HC-2.5 (Figure 4B). Such a trend suggests that increasing temperature led to the improvement of the capacitive characteristics of the supercapacitor cells. Similar trend is also observed for the supercapacitor cells made from the ACMSs of other HC-xs. This behavior is likely associated with the decrease of the resistance to the migration of electrolyte ions at high temperatures, allowing for rapid migration of electrolyte ions to the active sites in the ACMSs. However, there is no correlation between the slope of the straight lines in the low-frequency region and the size of the ACMSs of HC-xs at 273 and 333 K, as shown in Figure 4C,D, as well as other temperatures, indicating the negligible effect of the size of the ACSs of similar porous structures on the capacitive behavior of the supercapacitor cells in the low frequency region.

According to Figure 5A, the Nyquist plots for the supercapacitors made from the ACMSs of AC-1 almost overlap with each other over a wide range of temperature. There is only a slight transition from the intermediate-frequency segment to the low-frequency segment. Such a trend indicates that the ACMSs of AC-1 exhibited less favorable capacitive characteristics in the temperature range, which is relatively insensitive to the testing temperature.

Contrary to the Nyquist plots of the supercapacitor cells made from the ACMSs of AC-1, there exists a significant change in the slope from the intermediate-frequency segment to the low-frequency segment for the supercapacitor cells made from the ACMSs of AC-12 (Figure 5B). The low-frequency segments for the supercapacitor cells made from the ACMSs of AC-12 in the temperature range of 273 to 333 K are nearly

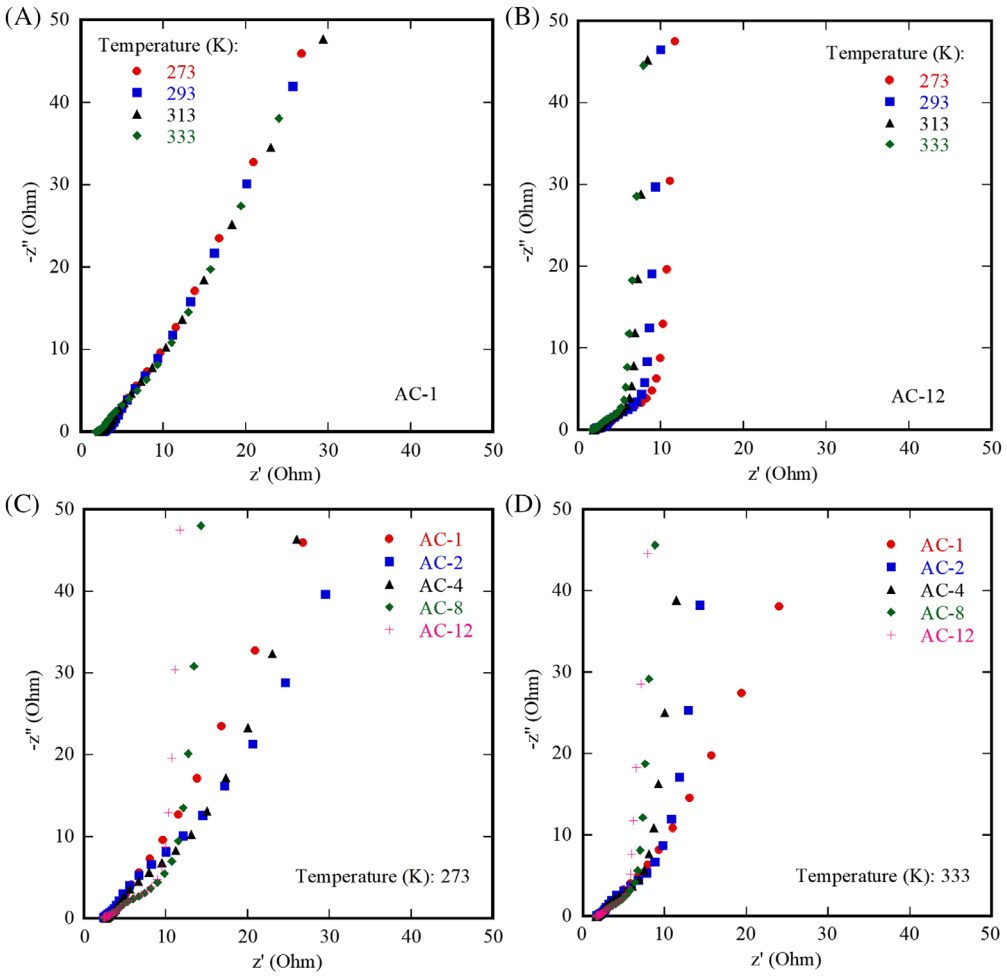

FIGURE 5 Nyquist plots of the symmetrical cells made from the ACMSs of: A, AC-1 and, B, AC-12 at different temperatures; Nyquist plots of the symmetrical cells made from the ACMSs of AC-*as* at temperatures of: C, 273 K and, D, 333 K [Colour figure can be viewed at wileyonlinelibrary.com]

TABLE 2 R_s of the ACMSs at different temperatures

Temperature (K)			273	293	313	333
HC-40	Average diameter (μm)	9.45	3.29	2.65	2.21	1.9
HC-20		5.79	3.22	2.88	2.76	2.15
HC-10		4.91	2.92	2.57	2.03	1.89
HC-5		3.69	2.97	2.77	2.37	2.13
HC-2.5		2.7	3.34	3.06	2.62	2.13
AC-1	Average pore width (nm)	1.61	2.72	2.67	2.26	1.81
AC-2		1.75	2.34	2.15	1.95	1.67
AC-4		1.79	2.43	2.15	2.11	1.59
AC-8		1.92	2.41	2.26	1.88	1.63
AC-12		2.02	2.38	1.99	1.82	1.58

parallel to the z″-axis, and the slope of the steep straight lines increases with the increase of temperature. The supercapacitor cells made from the ACMSs of AC-12 exhibited much better capacitive characteristics than those made from the ACMSs of AC-1, revealing the important role of the porous structure (pore width/size and distribution of pore width/size) of ACMSs in determining electrochemical performance. The smaller pore width of the ACMSs of AC-1 makes it difficult for relatively large electrolyte ions to migrate/diffuse in micropores, and the larger pores pore size/width of the ACMSs of AC-12 facilitates the migration/diffusion of electrolyte ions in micropores even at low temperatures.

The effect of the pore width/size on the capacitive characteristics of the supercapacitor cells is illustrated in

Figure 5C,D at two temperatures of 273 and 333 K. At temperature of 273 K, the supercapacitors made from the ACMSs of AC-8 and AC-12 have significantly larger slopes of the low-frequency segment than those made from the ACMSs with relatively smaller pores (AC-1, AC-2, and AC-4). At temperature of 333 K, all the supercapacitors except those made from the ACMSs of AC-1 exhibited good capacitive characteristics. Such results reveal that the electrochemical performance of the carbon-carbon supercapacitor cells is temperature-dependent. Increasing temperature increases the migration rate of electrolyte ions and the pore width/size, and there are more micropores accessible to electrolyte ions for the energy storage at high temperatures. ACMSs with relatively large pores benefit the energy storage in EDL over a broad range of temperature and are good candidates for practical applications. Note that the R_s value exhibits a decreasing trend with the increase of the average pore width/size, as shown in Table 2, which also contributes to the increase in the energy storage.

4 | DISCUSSION

It is known that one can calculate the apparent diffusivity of electrolyte ions in a chemical system from the EIS analysis. Note that the apparent diffusivity is associated with the mobility of electrolyte ions under open circuit, corresponding to the equilibrium state for symmetric cells, which likely is different from those under the action of a large, external field.

Following the method used in lithium-ion battery,[44,45] the apparent diffusivity of electrolyte ions, D, in a symmetrical supercapacitor cell under open circuit can be calculated as[41]

$$D = \frac{R^2T^2}{2An^4F^4C^2\sigma^2} \quad (1)$$

where, R T, A, n, F, and C are the gas constant ($8.314\ J \cdot K^{-1} \cdot mol^{-1}$), absolute temperature, electrode area, ionic charge, Faraday constant ($96\,500\ C \cdot mol^{-1}$), and ionic concentration, respectively. The parameter, σ, is the Warburg factor, which is $z'/(1/\omega^{-0.5})$ (z' is the real part of electrochemical impedance, and ω is frequency), as determined from the intermediate-frequency region in the Nyquist plots.

Figure 6 presents the variation of z' with $\omega^{-0.5}$ for the ACMSs of HC-xs at different temperatures. It is evident that z' is a linearly increasing function of $\omega^{-0.5}$, as expected. Using linear regression to fit the data in Figure 6, we obtain the σ values, which are summarized in Table 3. Substituting the σ values in Equation (1), we calculate the apparent diffusivity for the ionic diffusion in the supercapacitor cells made from the ACMSs of HC-xs.

Figure 7A shows the temperature dependence of the apparent diffusivities for the diffusion of electrolyte ions in the supercapacitor cells made from the ACMSs of HC-xs. It is evident that increasing temperature increases the apparent diffusivity for the same group of supercapacitor cells. In general, the apparent diffusivity is proportional to the mobility of electrolyte ions, μ, whose temperature dependence follows the Arrhenius relationship. Thus, the temperature dependence of the apparent diffusivities can be expressed as

$$D = D_0 e^{-Q/RT} \quad (2)$$

in which D_0 is a pre-factor, and Q is the apparent activation energy of the rate process. Using Equation (2) to curve-fit the data in Figure 7A, we obtain the pre-factor of D_0 and the apparent activation energy of Q. For comparison, the fitting curves are also included in Figure 7A. It is evident that the apparent diffusivity for the migration/diffusion of electrolyte ions in the supercapacitor cells made from the ACMSs of HC-xs indeed follows the Arrhenius-type relationship.

Figure 7B depicts the dependence of the apparent activation energy of Q and the pre-factor of D_0 on the average size of the ACMSs for the migration/diffusion of electrolyte ions in the supercapacitor cells made from the ACMSs of HC-xs. Both the apparent activation energy of Q and the pre-factor of D_0 increase nonlinearly with the increase of the average size of the ACMSs of HC-xs. Such behavior can be attributed to that the local concentration of electrolyte ions in the micropores of a larger ACS is likely larger than that in the micropores of a smaller ACS, resulting in the increase of the number of electrolyte ions available to move from one position to an adjacent position (crowding effect), that is, the increase in D_0, and the increase of the interaction between electrolyte ions to hinder the ionic diffusion (overscreening effect), that is, the increase of the energy barrier for the diffusion/migration of the electrolyte ions. There exists size effect on the diffusion/migration of the electrolyte ions in the supercapacitor cells made from the ACMSs of nearly same porous structure.

From Figure 5, we determine the correlation between z' and $1/\omega^{-0.5}$, as shown Figure 8, for the supercapacitor cells made from the ACMSs of AC-*a*s at different temperatures in the intermediate-frequency region. Similar to the supercapacitor cells made from the ACMSs of HC-xs, z' is a linearly increasing function of $\omega^{-0.5}$. Using linear regression to fit the data in Figure 8, we obtain the values of σ for the supercapacitor cells made from the ACMSs of AC-*a*s, which

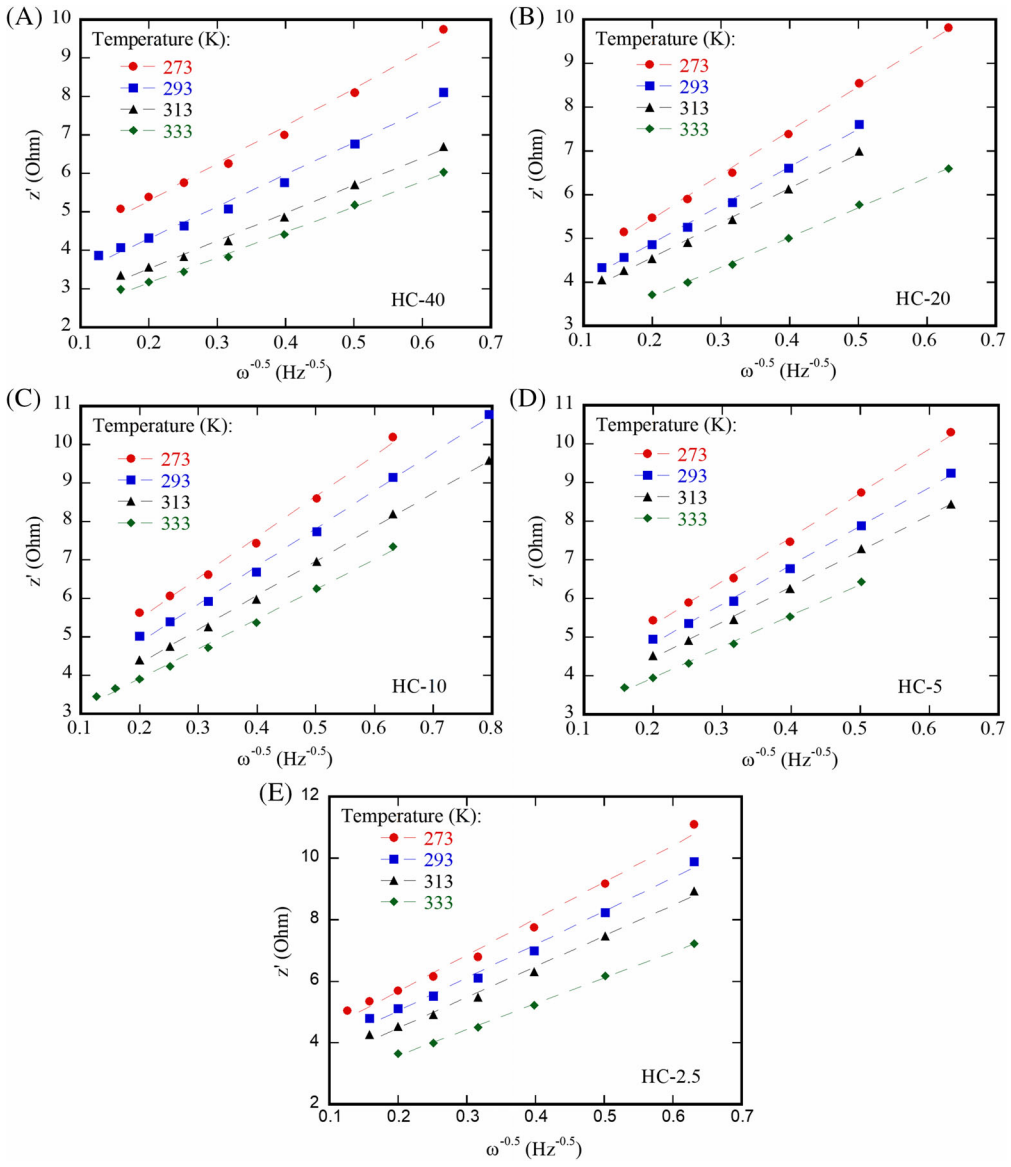

FIGURE 6 Dependence of z' on $\omega^{-0.5}$ for the supercapacitor cells made from the ACMSs of HC-xs at different temperatures. A, HC-40. B, HC-20. C, HC-10. D, HC-5. E, HC-2.5 [Colour figure can be viewed at wileyonlinelibrary.com]

TABLE 3 Values of σ for the supercapacitor cells made from the ACMSs

	Temperature (K)			273	293	313	333
HC-40	σ (ohm·Hz$^{1/2}$)	Average size of activated carbon spheres (μm)	9.45	9.7	8.3	7.2	6.6
HC-20			5.79	10.0	8.6	7.8	6.9
HC-10			4.91	11.1	9.8	8.9	7.7
HC-5			3.69	11.4	10.1	9.2	8.0
HC-2.5			2.70	11.8	10.8	9.9	8.6
AC-1	σ (ohm·Hz$^{1/2}$)	Average pore width (nm)	1.6	8.8	8.1	7	6.2
AC-2			1.75	7.9	6.9	6	5.1
AC-4			1.79	6.9	5.9	5.2	4.5
AC-8			1.92	5.2	4.4	3.9	3.6
AC-12			2.02	4.8	4.3	3.9	3.6

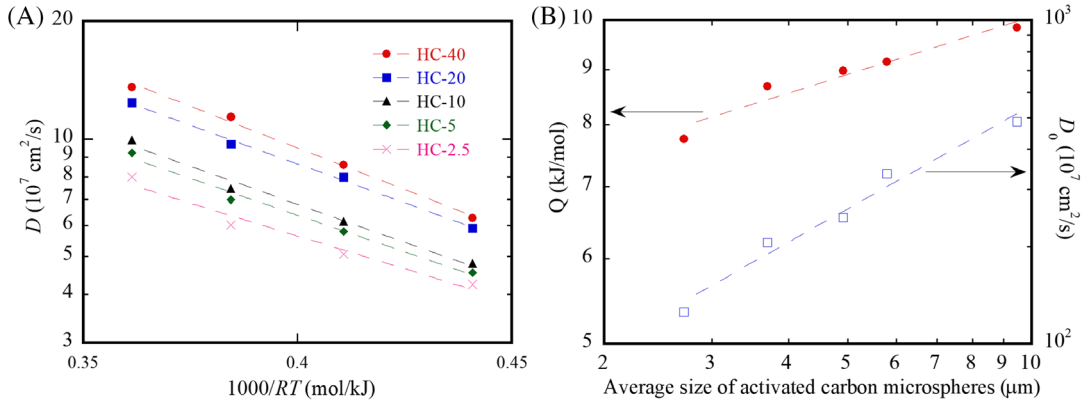

FIGURE 7 A, Temperature dependence of the apparent diffusivities for the migration/diffusion of electrolyte ions in the supercapacitors made from the ACMSs of HC-xs, and, B, variations of the apparent activation energy and pre-factor with average size of the ACMSs for the migration/diffusion of electrolyte ions in the supercapacitor cells made from the ACMSs of HC-xs [Colour figure can be viewed at wileyonlinelibrary.com]

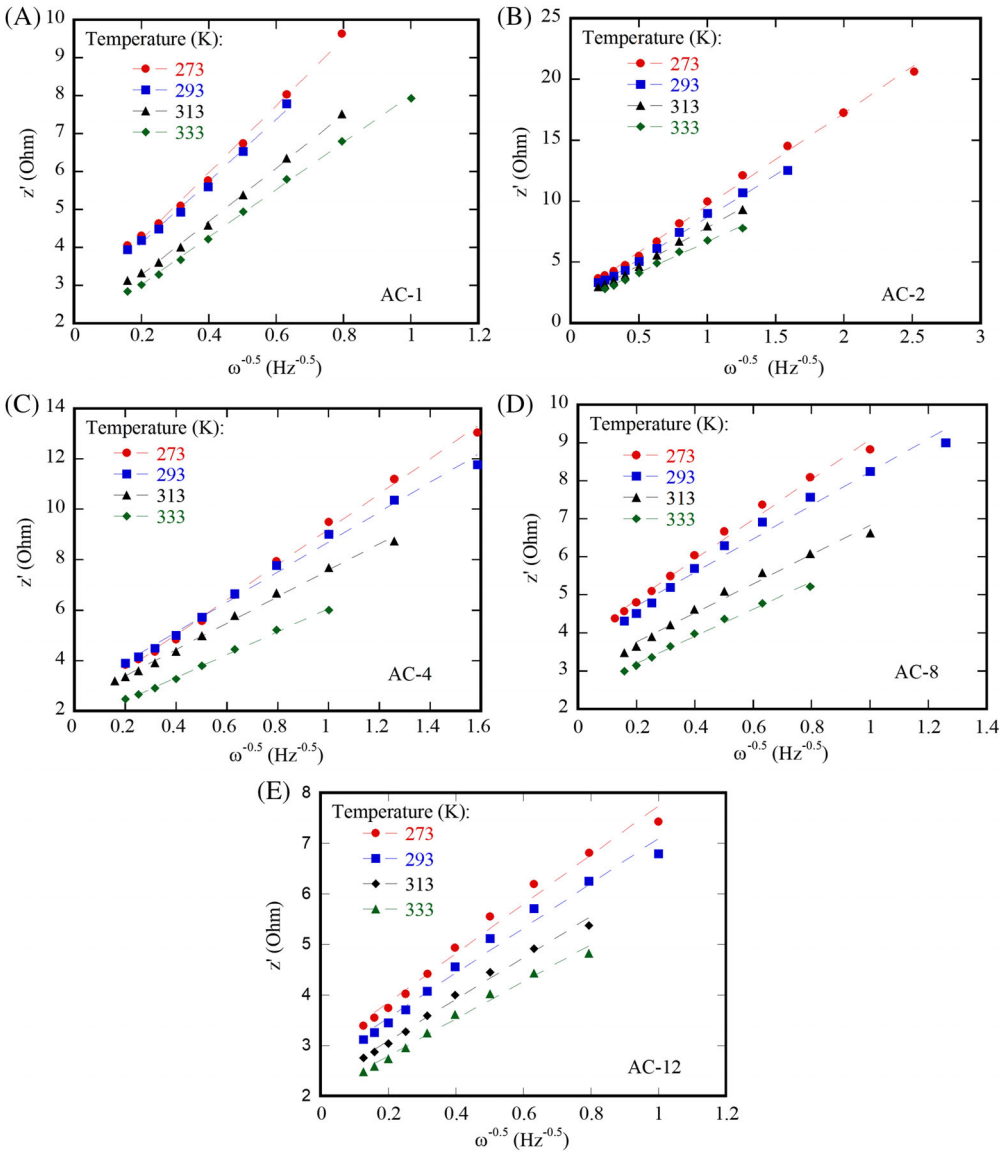

FIGURE 8 Relationships between z′ and $\omega^{-0.5}$ measured at different temperatures in the range of 273 to 333 K for: A, AC-1 and, B, AC-2, C, AC-4, D, AC-8, and, E, AC-12, respectively [Colour figure can be viewed at wileyonlinelibrary.com]

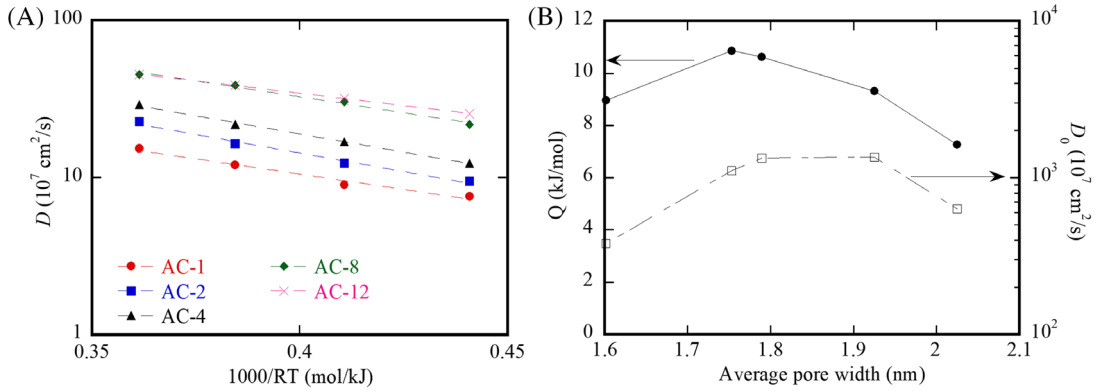

FIGURE 9 A, Dependence of the apparent diffusivity on temperature for the carbon spheres of AC-*a*, and, B, variation of the apparent activation energy with average pore width for the carbon spheres of AC-*a*s [Colour figure can be viewed at wileyonlinelibrary.com]

are summarized in Table 3. Substituting the values of σ in Equation (1), we calculate the apparent diffusivities for the migration/diffusion of electrolyte ions in the supercapacitor cells made from the ACMSs of AC-*a*s.

Figure 9A presents the temperature dependence of the apparent diffusivity for the diffusion of electrolyte ions in the supercapacitor cells made from the ACMSs of AC-*a*s. The apparent diffusivity for the same group of supercapacitors increases with the increase of temperature, as expected. At the same temperature, the apparent diffusivity increases with the increase of the average pore width. Such a trend is likely due to steric effect. The confinement of micropores to the diffusion of electrolyte ions reduces the speed/rate of electrolyte ions. Increasing the pore width allows for fast diffusion of electrolyte ions under the same driving force at the same temperature.

Using Equation (2) to curve-fit the data in Figure 9A, we obtain the pre-factor of D_0 and the apparent activation energy of Q. For comparison, the fitting curves are also included in Figure 9A. It is evident that the apparent diffusivity for the ionic diffusion in the supercapacitor cells made from the ACMSs of AC-*a*s also follows the Arrhenius-type relationship.

Figure 9B depicts the dependence of the apparent activation energy of Q and the pre-factor of D_0 on the average pore width of the ACMSs for the ionic diffusion in the supercapacitor cells made from the ACMSs of AC-*a*s. The apparent activation energy increases first and then decreases with the increase of the average pore width in contrast to the increasing trend of the apparent activation energy for the ionic diffusion in the supercapacitor cells made from the ACMSs of HC-xs. The pre-factor also exhibits similar trend to the apparent activation energy except that the pre-factor reaches maximum at the average pore width different from that for the corresponding apparent activation energy. The mechanism controlling this behavior is unclear and may be dependent on the combined effect of the average pore width and the distribution of pore widths. It needs to be pointed out that ionic diffusion in nanoporous materials[46] is also likely dependent on porous roughness, which needs to be incorporated in the analysis.

It is known that the characteristic time, τ_0, which is determined at the phase angle of ~45 ° in the Bode plot,[47] represents the diffusion characteristics of ions under electrochemical cycling. The smaller the characteristic time, the larger is the migration rate (diffusivity) of the ions. Table 4 lists the values of τ_0 for the supercapacitor cells made from the ACMSs at different temperatures. The characteristic time decreases generally with the increase of the temperature, indicating faster diffusion of ions at a higher temperature. Such a trend is in agreement with that shown in Figure 9A.

For the supercapacitor cells made from the ACMSs of HC-x, the characteristic time decreases with increasing the average size of ACMSs. For the supercapacitor cells made from the ACMSs of AC-*a*s, increasing the average pore width/size decreases the characteristic time. These results reveal the dependence of the ionic migration/diffusion in ACMSs under electrochemical cycling on the size and porous structures of ACMSs. The larger the size and pore width/size of AMCSs, the smaller is the characteristic time, and the larger is the migration rate/diffusivity of ions. These trends are in agreement with the trend obtained from the analysis of the apparent diffusivity, even though the characteristic time is determined from a single frequency and the Warburg factor is determined from a frequency range. Such a result supports that large size and pore width/size of AMCSs is likely to facilitate ionic migration/diffusion during electrochemical cycling.

	Temperature (K)			273	293	313	333
HC-40	τ_0 (s)	Average size of ACSs (μm)	9.45	1	0.63	0.57	0.42
HC-20			5.79	1.33	1	0.66	0.63
HC-10			4.91	1.58	1.11	0.68	0.63
HC-5			3.69	1.58	1.17	0.68	0.63
HC-2.5			2.70	1.63	1.25	0.71	0.65
AC-1	τ_0 (s)	Average pore width (nm)	1.6	18.6	15.8	12.5	10
AC-2			1.75	15.8	12.5	10	8.78
AC-4			1.79	13.3	10	8.69	6.29
AC-8			1.92	12.5	10	8.3	5.39
AC-12			2.02	6.32	4.16	3.98	3.03

TABLE 4 Values of τ_0 for the supercapacitor cells made from the ACMSs

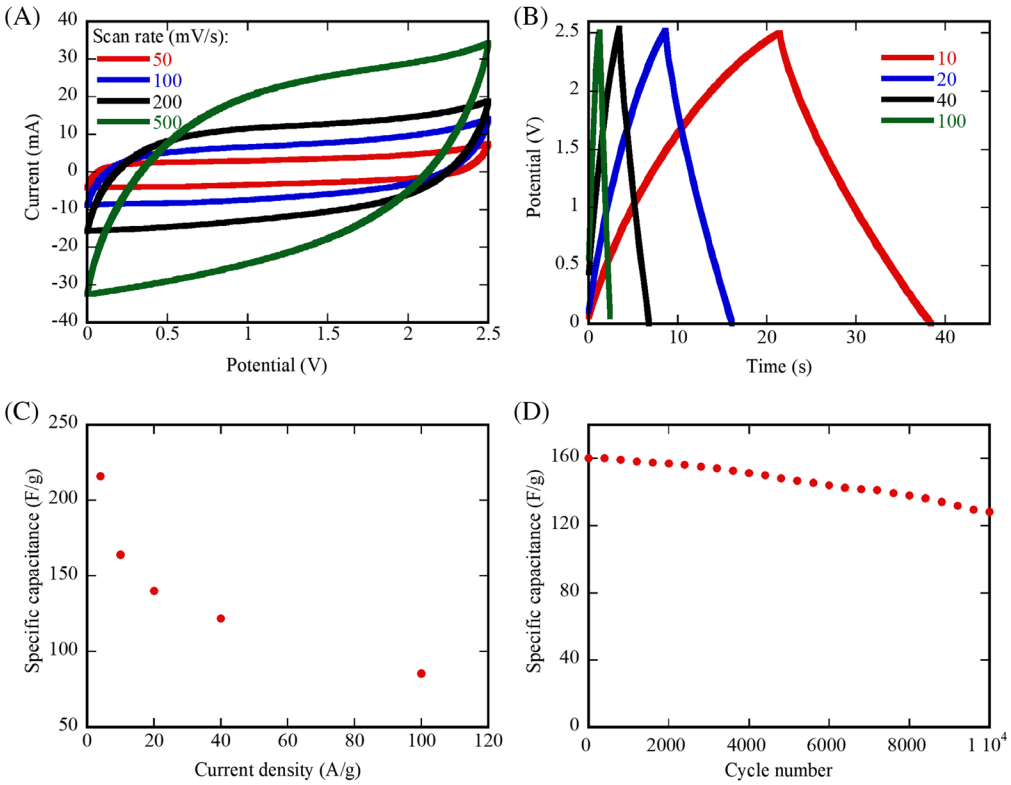

FIGURE 10 Electrochemical performance of the supercapacitor cells with the ACMSs of AC-12 as the electrode material: A, cyclic voltammetry (CV) curves measured at different scan rates, B, galvanostatic charge/discharge (GCD) curves measured with different current densities, C, variation of specific capacitance with current density, and, D, cycling performance. All the measurements were conducted at 20°C [Colour figure can be viewed at wileyonlinelibrary.com]

For the potential application, we investigated the electrochemical performance of the carbon-carbon, symmetrical supercapacitor cells with the ACMSs of AC-12 as the electrode material in 1 mol/L Et4NBF4 solution in AN at 20°C. Note that the ACMSs of AC-12 possess the optimal surface characteristics and ionic migration/diffusion.

Figure 10A shows the cyclic voltammetry (CV) curves. The CV curve exhibits good quasi-rectangular shape for the scan rate up to 200 mV/s, indicating good capacitive behavior and fast charge-transfer rate. At an extremely high scan rate of 500 mV/s, the CV curve still maintains relatively "good" rectangular shape, suggesting the potential application of the ACMSs of AC-12 in ultrafast supercapacitors.

The galvanostatic charge/discharge (GCD) curves in Figure 10B exhibit symmetrical and linear characteristics at high current densities, revealing excellent capacitive behavior. Using the following equation, we calculated the specific capacitance per electrode.

$$C = \frac{2I}{m}\left(\frac{dV}{dt}\right)^{-1} \quad (3)$$

where I is the applied current passing though the supercapacitor cell, m is the total mass of ACMSs, and dV/dt is the slope of the discharge segment of the GCD curve after the IR drop. Figure 10C illustrates the variation of the specific capacitance per electrode with the current

density. It is evident that the ACMSs of AC-12 possess a high specific capacitance up to 220 F/g at a current density of 4 A/g and a considerable specific capacitance of 85 F/g at an extremely high current density of 100 A/g.

The cycling performance of the supercapacitor cells at a current density of 10 A/g is presented in Figure 10D. After 10 000 cycles, the supercapacitor cells retain 80.1% of the specific capacitance, suggesting good long-term stability. All these results demonstrate that the ACMSs of AC-12 can be used as the electrode material of supercapacitors for practical applications.

5 | SUMMARY

In summary, we have brought out the important role of the size and pore width/size of ACMSs in determining the electrochemical performance of carbon-carbon symmetrical supercapacitors in the framework of EIS. Using xylose as the precursor and the combination of hydrothermal carbonization and physical/chemical activation, we have prepared two groups of ACMSs: one group has similar porous structures and different sizes, and the other has approximately the same size and different porous structures. Carbon-carbon symmetrical supercapacitors with organic electrolyte have been assembled from the two groups of ACMSs. The EIS of the carbon-carbon symmetrical supercapacitor cells has been analyzed.

Increasing temperature decreases the R_s value of the supercapacitor cells. Both the size and pore width of the ACMSs have negligible effect on the contact resistance. The capacitive behavior of the supercapacitor cells made from the ACMSs of similar porous structures is independent of the size of the ACMSs. ACMSs with relatively large pores benefit the energy storage in EDL over a broad range of temperature and are good candidates for practical applications.

There exists size effect on the diffusion/migration of the electrolyte ions in the supercapacitor cells made from the ACMSs of nearly the same porous structure, which are likely attributed to overscreening and crowding effects. Both the apparent activation energy and the pre-factor for the migration/diffusion of electrolyte ions in the supercapacitor cells made from the ACMSs of nearly the same porous structure increase nonlinearly with the increase of the average size of the ACMSs. The apparent activation energy for the supercapacitor cells made from the ACMSs of nearly the same size increases first and then decreases with increasing the average pore width in contrast to the increasing trend of the apparent activation energy for the supercapacitor cells made from the ACMSs of nearly same porous structure. The pre-factor also exhibits similar trend to the apparent activation energy except the pre-factor reaches maximum at different average pore width.

ACKNOWLEDGEMENTS

Wei Sun is grateful for the support from the National Natural Science Foundation of China (No. 21805123), the Liao-Ning Revitalization Talents Program (XLYC1907067), and Talent Scientific Research Fund of LSHU (No. 2016XJJ-077). Fuqian Yang is grateful for the support from the NSF (CMMI-1634540), monitored by Drs. Khershed Cooper and Thomas Francis Kuech.

CONFLICT OF INTEREST

The authors declare that they have no known competing financial interests or personal relationships that could have appeared to influence the work reported in this paper.

AUTHOR CONTRIBUTIONS

Wei Sun: Experiment; data curation; writing – original draft. **Fuqian Yang:** Conceptualization, experimental design; writing – review & editing; supervision.

DATA AVAILABILITY STATEMENT

The data supporting the findings of this study are available upon request.

ORCID

Fuqian Yang https://orcid.org/0000-0001-6277-3082

REFERENCES

1. Wang G, Zhang L, Zhang J. A review of electrode materials for electrochemical supercapacitors. *Chem Soc Rev*. 2012;41:797-828.
2. Yang Z, Tian J, Yin Z, Cui C, Qian W, Wei F. Carbon nanotube- and graphene-based nanomaterials and applications in high-voltage supercapacitor: a review. *Carbon*. 2019;141:467-480.
3. Sun W, Lipka SM, Swartz C, Williams D, Yang F. Hemp-derived activated carbons for supercapacitors. *Carbon*. 2016;103:181-192.
4. Quan C, Su RR, Gao NB. Preparation of activated biomass carbon from pine sawdust for supercapacitor and CO_2 capture. *Int J Energy Res*. 2020;44:4335-4351.
5. Sharma P, Bhatti TS. A review on electrochemical double-layer capacitors. *Energy Convers Manag*. 2010;51:2901-2912.
6. Signorelli R, Ku DC, Kassakian JG, Schindall JE. Electrochemical double-layer capacitors using carbon nanotube electrode structures. *Proc IEEE*. 2009;97:1837-1847.
7. Brezesinski T, Wang J, Tolbert SH, Dunn B. Ordered mesoporous α-MoO_3 with iso-oriented nanocrystalline walls for thin-film pseudocapacitors. *Nat Mater*. 2010;9:146-151.
8. Zhai T, Wan L, Sun S, et al. Phosphate ion functionalized Co_3O_4 ultrathin nanosheets with greatly improved surface

reactivity for high performance pseudocapacitors. *Adv Mater*. 2017;29:1604167.
9. Shrivastav V, Sundriyal S, Kim KH, Sinha RK, Tiwari UK, Deep A. Metal-organic frameworks-derived titanium dioxide-carbon nanocomposite for supercapacitor applications. *Int J Energy Res*. 2020;44:6269-6284. https://doi.org/10.1002/er.5328.
10. Cevik E, Bozkurt A. Design of high-performance flexible symmetric supercapacitors energized by redox-mediated hydrogels including metal-doped acidic polyelectrolyte. *Int J Energy Res*. 2020;44:4309-4320.
11. Stoller MD, Ruoff RS. Best practice methods for determining an electrode material's performance for ultracapacitors. *Energy Environ Sci*. 2010;3:1294-1301.
12. Yang W, Feng Y, Xiao D, Yuan H. Fabrication of microporous and mesoporous carbon spheres for high-performance supercapacitor electrode materials. *Int J Energy Res*. 2015;39:805-811.
13. Pandolfo AG, Hollenkamp AF. Carbon properties and their role in supercapacitors. *J Power Sources*. 2006;157:11-27.
14. Zhu Y, Murali S, Stoller MD, et al. Carbon-based supercapacitors produced by activation of graphene. *Science*. 2011; 332:1537-1541.
15. Biswas S, Drzal LT. Multi-layered nanoarchitecture of graphene nanosheets and polypyrrole nanowires for high performance supercapacitor electrodes. *Chem Mater*. 2010;22: 5667-5671.
16. Wang SS, Sun W, Yang DS, Yang FQ. Conversion of soybean waste to sub-micron porous-hollow carbon spheres for supercapacitor via a reagent and template-free route. *Mater Today Energy*. 2019;13:50-55.
17. Hong P, Liu X, Zhang X, et al. Hierarchically porous carbon derived from the activation of waste chestnut shells by potassium bicarbonate ($KHCO_3$) for high-performance supercapacitor electrode. *Int J Energy Res*. 2019;44:988-999. https://doi.org/10.1002/er.4970.
18. Yang HW, Zhou J, Wang MQ, Wu SJ, Yang W, Wang H. From basil seed to flexible supercapacitors: green synthesis of heteroatom-enriched porous carbon by self-gelation strategy. *Int J Energy Res*. 2020;44:4449-4463.
19. Zhou P, Wan JF, Wang XR, Xu K, Gong YG, Chen LN. Nickel and cobalt metal-organic-frameworks-derived hollow microspheres porous carbon assembled from nanorods and nanospheres for outstanding supercapacitors. *J Colloid Interface Sci*. 2020;575:96-107.
20. Liu KL, Wang JZ, Yang T, Wang H, Wang CY, Chen MM. An "in situ templating" strategy towards mesoporous carbon for high-rate supercapacitor and high adsorption capacity on dye macromolecules. *Carbon*. 2020;164:19-27.
21. An KH, Kim WS, Park YS, et al. Supercapacitors using single-walled carbon nanotube electrodes. *Adv Mater*. 2001;13:497-500.
22. Guo NN, Luo WX, Guo RH, et al. Interconnected and hierarchical porous carbon derived from soybean root for ultrahigh rate supercapacitors. *J Alloys Compd*. 2020;834:155115.
23. Rajesh M, Manikandan R, Park S, et al. Pinecone biomass-derived activated carbon: the potential electrode material for the development of symmetric and asymmetric supercapacitors. *Int J Energy Res*. 2020. https://doi.org/10.1002/er.5548.
24. Zhou W, Yang F. Integral capacitance of diffusion layer for rectangular structures article reference. *J Energy Storage*. 2020; 30:101477.
25. Wang K, Zhao N, Lei SW, et al. Promising biomass-based activated carbons derived from willow catkins for high performance supercapacitors. *Electrochim Acta*. 2015;166:1-11.
26. Yang W, Yang W, Kong LN, Song AL, Qin XJ, Shao GJ. Phosphorus-doped 3D hierarchical porous carbon for high-performance supercapacitors: a balanced strategy for pore structure and chemical composition. *Carbon*. 2018;127:557-567.
27. Chaudhary S, Kumar A, Sharma ND, Gupta M. Cauliflower-shaped ternary nanocomposites with enhanced power and energy density for supercapacitors. *Int J Energy Res*. 2019;43: 3446-3460.
28. Wang Y, Shi Z, Huang Y, et al. Supercapacitor devices based on graphene materials. *J Phys Chem C*. 2009;113:13103-13107.
29. Wang H, Xu Z, Kohandehghan A, et al. Interconnected carbon nanosheets derived from hemp for ultrafast supercapacitors with high energy. *ACS Nano*. 2013;7:5131-5141.
30. Chen AB, Yu YF, Xing TT, Wang RJ, Zhang Y, Li Q. Synthesis of graphitic carbon spheres for enhanced supercapacitor performance. *J Mater Sci*. 2015;50:5578-5582.
31. Huang CH, Zhang Q, Chou TC, Chen CM, Su DS, Doong RA. Three-dimensional hierarchically ordered porous carbons with partially graphitic nanostructures for electrochemical capacitive energy storage. *ChemSusChem*. 2012;5:563-571.
32. Zhao Q, Tao S, Miao X, Zhu Y. A green, rapid, scalable and versatile hydrothermal strategy to fabricate monodisperse carbon spheres with tunable micrometer size and hierarchical porosity. *Chem Eng J*. 2019;372:1164-1173.
33. Li M, Li W, Liu SX. Hydrothermal synthesis, characterization, and KOH activation of carbon spheres from glucose. *Carbohydr Res*. 2011;346:999-1004.
34. Jagiello J, Kenvin J, Celzard A, Fierro V. Enhanced resolution of ultra micropore size determination of biochars and activated carbons by dual gas analysis using N_2 and CO_2 with 2D-NLDFT adsorption models. *Carbon*. 2019;144:206-215.
35. Jagiello J, Thommes M. Comparison of DFT characterization methods based on N_2, Ar, CO_2, and H_2 adsorption applied to carbons with various pore size distributions. *Carbon*. 2004;42: 1227-1232.
36. Huang G-G, Liu Y-F, Wu X-X, Cai J-J. Activated carbons prepared by the KOH activation of a hydrochar from garlic peel and their CO_2 adsorption performance. *New Carbon Mater*. 2019;34:247-257.
37. Guo F, Jia X, Liang S, Jiang X, Peng K, Qian L. Design and synthesis of highly porous activated carbons from Sargassum as advanced electrode materials for supercapacitors. *J Electrochem Soc*. 2019;166:A3109.
38. Wei H, Wang H, Li A, et al. Advanced porous hierarchical activated carbon derived from agricultural wastes toward high performance supercapacitors. *J Alloys Compd*. 2020;820: 153111.
39. Kim Y-J, Lee B-J, Suezaki H, et al. Preparation and characterization of bamboo-based activated carbons as electrode materials for electric double layer capacitors. *Carbon*. 2006;44:1592-1594.
40. Wickramaratne NP, Xu JT, Wang M, Zhu L, Dai LM, Jaroniec M. Nitrogen enriched porous carbon spheres: attractive materials for supercapacitor electrodes and CO_2 adsorption. *Chem Mater*. 2014;26:2820-2828.
41. Sun W, Zhang YL, Yang ZX, Yang FQ. High-performance activated carbons for electrochemical double layer capacitors:

effects of morphology and porous structures. *Int J Energy Res*. 2020;44:1930-1950.
42. Kang S, Li X, Fan J, Chang J. Characterization of hydrochars produced by hydrothermal carbonization of lignin, cellulose, D-xylose, and wood meal. *Ind Eng Chem Res*. 2012;51:9023-9031.
43. Farma R, Deraman M, Awitdrus TIA, et al. Physical and electrochemical properties of supercapacitor electrodes derived from carbon nanotube and biomass carbon. *Int J Electrochem Sci*. 2013;8:257-273.
44. Yoo E, Nakamura J, Zhou H. N-doped graphene nanosheets for Li-air fuel cells under acidic conditions. *Energy Environ Sci*. 2012;5:6928-6932.
45. Yu L, Falco C, Weber J, White RJ, Howe JY, Titirici M-M. Carbohydrate-derived hydrothermal carbons: a thorough characterization study. *Langmuir*. 2012;28:12373-12383.
46. Malek K, Coppens M-O. Pore roughness effects on self-and transport diffusion in nanoporous materials. *Colloids Surf A Physicochem Eng Asp*. 2002;206:335-348.
47. Liu T, Liu JH, Zhang LY, Cheng B, Yu JG. Construction of nickel cobalt sulfide nanosheet arrays on carbon cloth for performance-enhanced supercapacitor. *J Mater Sci Technol*. 2020;47:113-121.

How to cite this article: Sun W, Yang F. Geometrical effects on ionic diffusion in carbon-carbon symmetric supercapacitors. *Int J Energy Res*. 2020;1–15. https://doi.org/10.1002/er.5863